





COMPARATIVE ANALYSIS OF FLOW PATTERNS IN OFF-DESIGN PLANAR AND CONICAL NOZZLE

ANÁLISIS COMPARATIVO DE PATRONES DE FLUJO EN TOBERAS PLANAS Y CÓNICAS FUERA DE DISEÑO

San L. Tolentino^{1,*} , Jorge Mirez¹ 

Received: 27-10-2024, Received after review: 03-12-2024, Accepted: 09-12-2024, Published: 01-01-2025

Abstract

This study aims to analyze the behavior of Mach number and pressure field flow patterns in off-design planar and conical nozzles with a divergent half-angle of 10.85°. Numerical simulations of the flow field were conducted using the ANSYS-Fluent R16.2 software, employing the RANS model and the SAS turbulence model under transient flow conditions. The nozzle pressure ratios (NPR) ranged from 1.97 to 8.91. The results reveal differences in flow patterns, including Mach number and static pressure, between the two nozzle types. Notably, normal shock fronts exhibited varying positions for the same NPR values. The maximum peak flow fluctuation along the centerline of the conical nozzle's divergent section reached Mach 2.844, compared to Mach 2.011 in the planar nozzle, indicating lower flow velocity in the latter. At the nozzle outlet, the flow velocity of the conical nozzle was Mach 2.535, representing a 27.32% increase compared to the planar nozzle, which achieved Mach 1.991. Additionally, the throat area significantly influenced mass flow transit, with the planar nozzle having a larger throat area than the conical nozzle. These findings provide insights into the impact of nozzle geometry on flow characteristics under off-design conditions.

Keywords: Flow fluctuations, RANS model, SAS turbulence model, Shock wave, Flow patterns, Off-design nozzles.

Resumen

En el presente trabajo, el objetivo es determinar el comportamiento de los patrones de flujo del campo de número de Mach y de presión para toberas planas y cónicas fuera de diseño, para el semiángulo de la divergente de 10,85°. Se empleó el código ANSYS-Fluent R16.2 para simular el campo de flujo con el modelo RANS y el modelo de turbulencia SAS para las condiciones de flujo en estado transitorio, para el rango de relaciones de presión de la tobera de NPR 1,97 a 8,91. Los resultados presentan diferentes patrones de flujo de número de Mach y de presión estática entre ambas toberas, donde los frentes de choque normales no tienen las mismas posiciones para un mismo valor de NPR. El pico máximo de la fluctuación del flujo en la línea central de la divergente de la tobera cónica es Mach 2,844, mientras que en la tobera plana es Mach 2,011, por lo que la velocidad del flujo es menor en la tobera plana. La velocidad del flujo a la salida de la tobera cónica es Mach 2,535, la cual es 27,32 % mayor que la velocidad del flujo en la tobera plana, que tiene Mach 1,991. El área de la garganta de la tobera tiene un efecto significativo para el tránsito del flujo másico, ya que el área de la garganta de la tobera plana es mayor con respecto al de la tobera cónica.

Palabras clave: fluctuaciones de flujo, modelo RANS, modelo de turbulencia SAS, onda de choque, patrones de flujo, toberas fuera de diseño

^{1,*}Group of mathematical modeling and numerical simulation, Universidad Nacional de Ingeniería, Lima, Perú.
Corresponding author ✉: stolentino@unexpo.edu.ve.

Suggested citation: Tolentino, S.L. and Mirez, J. "Comparative analysis of flow patterns in off-design planar and conical nozzle," *Ingenius, Revista de Ciencia y Tecnología*, N.º 33, pp. 115-127, 2025, DOI: <https://doi.org/10.17163/ings.n33.2025.10>.

1. Introduction

The geometries of convergent-divergent nozzles used in the aerospace field significantly influence the development of the flow field. Consequently, the geometry of the nozzle's inner wall and the resulting flow turbulence remain recurring topics of interest, particularly under overexpanded, adapted, and under expanded viscous flow conditions [1]. Since the advent of technological advancements in supersonic nozzles, their geometries have undergone continuous evolution to optimize and regulate flow transit. Among the prominent nozzle geometries are conical nozzles, contoured or bell-shaped designs (both full-length and shortened), plug or aerospike nozzles (full-length and truncated), expansion-deflection nozzles, planar nozzles, and others [1–6]. Research in this area has extended to the method of characteristics (MOC) [7, 8], as well as the development of approximate mathematical models to simulate flow using computational fluid dynamics (CFD) tools [9, 10]. Furthermore, studies have explored the solution of mathematical models for isentropic flow involving analytical equations that cannot be inverted through algebraic procedures [11–14].

Supersonic conical nozzles with optimal performance typically have a divergent half-angle α ranging from 12° to 18° . When $\alpha < 12^\circ$, these nozzles are classified as off-design [1]. The same principle applies to planar nozzles with no curvature in the divergent section.

Under overexpanded flow conditions, various shock wave phenomena occur in the divergent section of the nozzle, including normal, oblique, reflected, and internal shock waves. Figure 1 illustrates the shock wave structure in the divergent section of a supersonic nozzle [15], along with an image of a shock wave captured using the Schlieren technique, as reported by Hunter [6], [16].

The central flow region contains the shock front, flanked by oblique and reflected waves that interact with pressure and temperature gradients [6], [17, 18]. In the flow region adjacent to the nozzle walls, lateral pressure loads are observed before and after the shock. The boundary layer interacts with the shock waves, and downstream of the flow separation point, backpressure and flow recirculation occur, accompanied by the formation of vortices. The effects of temperature and friction are prominent in the flow region near the walls, where free shock separation (FSS) and restricted shock separation (RSS) phenomena are observed [19–22]. At the nozzle's edges, such as the exit edge, Prandtl-Meyer expansion waves occur [17]. The supersonic jet flow discharged into the atmosphere forms a plume containing shock wave structures, which are influenced by the nozzle pressure ratio (NPR) [19].

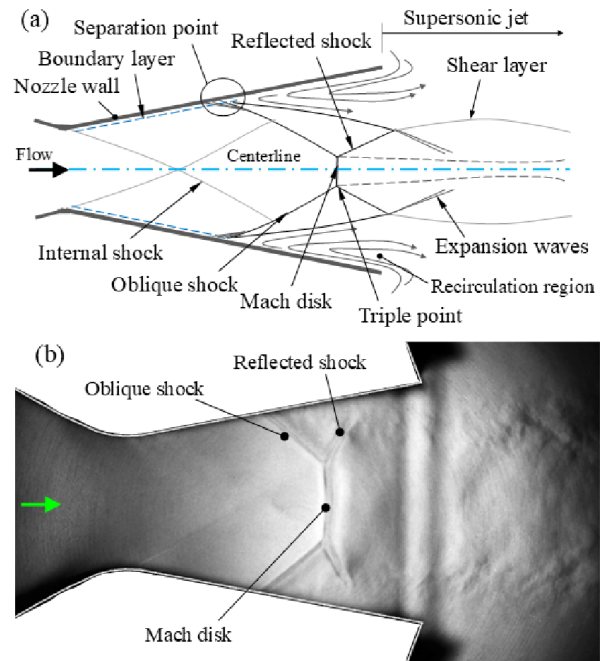


Figure 1. (a) Shock wave structure for the overexpanded flow condition [15]. (b) Experimental image of the shock wave structure in a planar nozzle, as reported by Hunter [6]

Several significant studies have explored the behavior of flow in off-design nozzles. Hunter [6] carried out experimental tests on flow separation in a planar nozzle with a divergent angle $\alpha = 11,01^\circ$, revealing that overexpanded flow was dominated by shock-induced boundary layer separation. Likewise, Verma and Mani Sankar [18] investigated planar nozzles with divergent angles $\alpha = 5,7^\circ$, $\alpha = 7,5^\circ$ and $\alpha = 10,7^\circ$, identifying asymmetry in normal, oblique, and reflected shock wave fronts, as well as non-symmetric boundary layer separation between the top and bottom walls. Tolentino et al. [23] conducted computational simulations for planar nozzles with $\alpha = 9^\circ$, $\alpha = 11,01^\circ$ and $\alpha = 13^\circ$, reporting that increasing the divergent angle led to increased flow velocity in the central region at the nozzle outlet. Arora and Vaidyanathan [24] investigated planar nozzles with double divergence, finding that the angle of inflection significantly influenced the shock structure, with additional expansion occurring at the second divergence.

Tolentino et al. [25] simulated the flow field in planar nozzles with a straight cutthroat for $\alpha = 11,01^\circ$. They found that as throat length increased, the shock train evolved within the throat section, affecting flow development in the divergent.

Mason et al. [26] experimentally studied planar nozzles with divergent angles $\alpha = 1,21^\circ$, $\alpha = 10,85^\circ$ and $\alpha = 11,24^\circ$. Their results showed that the convergent and throat contour significantly affected flow behavior. For $\alpha = 1,21^\circ$, pressure fluctuations were observed along the divergent wall due to the presence of a shock train. In contrast, for $\alpha = 10,85^\circ$, only a pressure jump

at the flow separation point was observed due to the normal shock front.

Tolentino et al. [15] studied conical nozzles with a straight-cut throat for $\alpha = 10^\circ$, showing that increasing throat length led to the evolution of the shock train and a reduction in thrust at the nozzle exit. Tolentino and Mirez [27] further analyzed flow patterns in conical nozzles, revealing that an optimal throat length prevents the formation of a shock train.

Other experimental studies have also investigated flow behavior in nozzles. Wagner and Schleichriem [28] examined flow turbulence in planar nozzles with wall curvature, reporting non-symmetric shock wave propagation. Bourgoing and Reijasse [29] demonstrated that wall roughness affects flow development, resulting in varying shock wave asymmetry configurations. Faheem et al. [30] conducted experiments with nozzles emitting multiple supersonic jets, finding that as the number of jets increased, the scattering rate decreased due to reduced drag, with notable differences in the cores of the supersonic jets.

Computational fluid dynamics (CFD) simulations [9] have proven effective in reproducing flow turbulence and determining thermodynamic parameters in regions where experimental imaging is not feasible. Recent research has focused on modeling turbulence for Mason et al.'s [26] experimental flat nozzle geometry, with extensions to conical nozzle geometries.

This study aims to analyze the behavior of flow patterns in planar and conical nozzles classified as off-design nozzles. Both nozzle types share identical geometric dimensions projected in a 2D computational domain. Section 2 outlines the methodology, including a description of the experimental nozzle geometry used by Mason et al. [26] to record pressure readings at different nozzle pressure ratios (NPR) under cold flow

conditions. The mathematical foundation and computational solution methods are also detailed, along with numerical convergence analysis and validation of the SAS turbulence model employed in simulations. Section 3 presents the numerical results, focusing on Mach number flow fields and static pressure distributions. Finally, Section 4 provides the conclusions of the analysis, summarizing the findings and their implications for future research.

2. Materials and method

2.1. Experimental nozzle

The experimental planar nozzle (Model B1) under study, as illustrated in Figure 2, was previously utilized by Mason et al. [26]. Pressure experiments for cold flow conditions were conducted at the NASA Langley Research Center's 16-Foot Transonic Tunnel Complex. These experimental tests covered a nozzle pressure ratio (NPR) range from 1.97 to 8.91. The planar nozzle [26] was designed for a Mach number of 2.08, an NPR of 8.81, an area ratio $A_e/A_t = 1,8$, and a divergent half-angle $\alpha = 10,85^\circ$, classifying it as an off-design nozzle since $\alpha < 12^\circ$. A_e represents the nozzle outlet area, and A_t denotes the throat area. The width of the planar nozzle is 10.157 cm.

It is noteworthy that the geometric dimensions of the planar nozzle, when projected onto a 2D plane (Figure 2a), are applied to the conical nozzle geometry. For the conical nozzle, the radii are defined as h_i for the inlet, h_t for the throat and h_e for the outlet, with a divergent half-angle $\alpha = 10,85^\circ$. The design conditions for the conical nozzle include a Mach number of 2.713, an NPR of 23.768, and an area ratio A_e/A_t of 3,224.

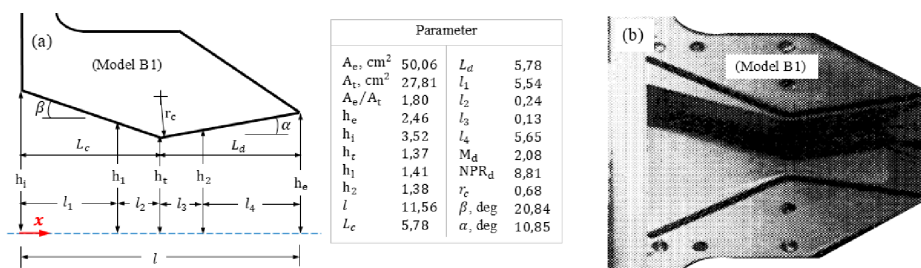


Figure 2. (a) Schematic representation of the planar nozzle, illustrating geometric parameters (units in centimeters). (b) Experimental planar nozzle used by Mason et al. [26] to measure the flow pressure along the inner walls

2.2. Computational domain

The spatial projection of the planar and conical nozzles was considered in 2D computational domains due to their symmetry. These domains were constructed using the geometric data reported by Mason et al. [26], as

depicted in Figure 2. Figure 3 illustrates the computational domain along with the meshed domain for Grid 4, which consists of 30,736 quadrilateral cells. Grid 4 represents a refined mesh with improved cell distribution, previously evaluated for performance compared to other meshed domains. The geometric dimensions are

parameterized, with the centerline aligned along the x -direction, and the divergent section denoted as L_d . The convergent section of the nozzle spans $0 \leq x/L_d \leq 1$, the divergent section spans $1 \leq x/L_d \leq 2$, and the atmosphere section extends from $2 \leq x/L_d \leq 8$. This computational domain setup is suitable for capturing the flow turbulence and simulating the formation

of the plume in the supersonic jet as it discharges into the atmosphere. It is important to note that 2D computational domains are appropriate for symmetric geometries, offering a significant reduction in iterative computational time and resource usage compared to 3D computational domains.

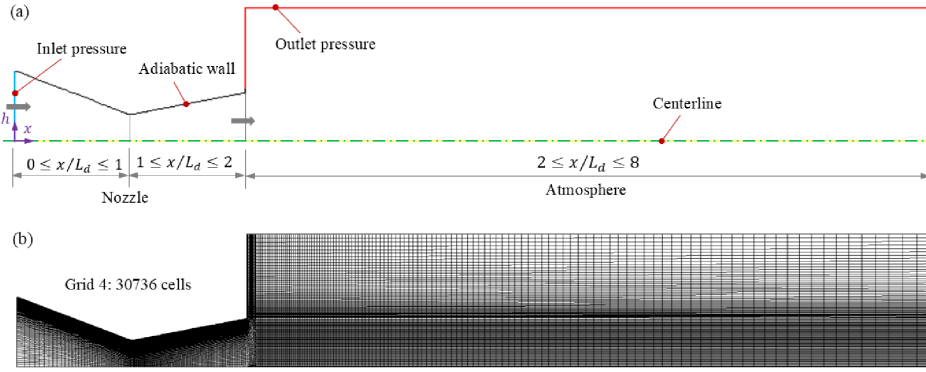


Figure 3. (a). 2D computational domain illustrating the applied boundary conditions (b) Structured mesh for Grid 4, consisting of 30736 quadrilateral cells

The boundary conditions applied to the 2D computational domain for both the planar and conical nozzles are as follows: At the nozzle inlet, stagnation pressure P_o data are specified for eight cases corresponding to nozzle pressure ratios (NPR) of 1.97, 2.94, 3.92, 4.88, 5.84, 6.81, 7.79, and 8.91, where $NPR = P_o/P$ and the pressure of the local atmosphere $P = 101,3$ kPa. The total temperature T_o is set to 300 K for all eight cases. At the nozzle outlet, the local atmospheric pressure and temperature are uniformly set to $P = 101,3$ kPa and $T = 300$ K for all cases. It is important to note that the pressure and temperature data were obtained from the work of Mason et al. [26].

The nozzle walls are modeled as adiabatic, meaning no heat transfer occurs through them. The mesh is refined in the regions adjacent to the walls to account for the presence of flow shear stresses. At the walls, the flow velocity is zero due to the no-slip condition. Along the centerline, the flow velocity is zero in the perpendicular direction for the planar nozzle and in the radial direction for the conical nozzle. The effects of gravity on flow turbulence are neglected, as the computational domains are two-dimensional and represent symmetric geometries.

The airflow is treated as an ideal gas with the following thermodynamic properties: gas constant $R = 287$ J/(kg·K), specific heat ratio $k = 1,4$, specific heat at constant pressure $C_p = 1006,43$ J/(kg·K) and thermal conductivity $k_t = 0,042$ W/(m·K) [31].

2.3. Mathematical fundamentals

The turbulence of the viscous flow field in a transient state is simulated using the ANSYS-Fluent R16.2 software [31], which employs the finite volume method (FVM) [9]. The Reynolds-Averaged Navier-Stokes (RANS) equations are utilized, as they provide an efficient and appropriate framework for obtaining approximate solutions to compressible flow turbulence. The governing equations for the calculation of compressible flow include the conservation of mass (Equation (1)), momentum (Equation (2)), and energy (Equation (3)) [9, 10], [31]. These equations, expressed in compact form, are as follows:

$$\frac{\partial \rho}{\partial t} + \nabla \cdot (\rho u_i) = 0 \quad (1)$$

$$\frac{\partial}{\partial t} (\rho u_i) + \nabla \cdot (\rho u_i u_j) = -\nabla p + \nabla \cdot (\bar{\tau}) + \nabla \cdot (-\rho \overline{u'_i u'_j}) \quad (2)$$

$$\frac{\partial}{\partial t} (\rho E) + \nabla \cdot (u_i (\rho E + p)) = \nabla \cdot (k_{eff} \nabla T + (\bar{\tau}_{eff} \cdot u_i)) \quad (3)$$

Where t is the time, ρ is the density, u is velocity, p is the pressure and $\bar{\tau}$ is the stress tensor. The term $-\rho \overline{u'_i u'_j}$ represents the Reynolds stress, where turbulence models are applied to close Equation (2). Additionally, E denotes the total energy, k_{eff} is the effective thermal conductivity, T is the temperature, and $\bar{\tau}_{eff}$ is the effective tensor.

The flow is modeled as an ideal gas; hence, the ideal gas equation of state (Equation (4)) is applied. The equations for pressure ratio (Equation (5)) and temperature (Equation (6)) are expressed as functions of the Mach number:

$$p = \rho RT \quad (4)$$

$$\frac{P_o}{P} = \left(1 + \frac{k-1}{2} M^2\right)^{\frac{k}{k-1}} \quad (5)$$

$$\frac{T_o}{T} = 1 + \frac{k-1}{2} M^2 \quad (6)$$

Where R is the universal ideal gas constant, P_o is the stagnation pressure, P is the static pressure, T_o is the stagnation temperature, T is the static temperature, and k is the ratio of specific heats. The Mach number, denoted as M , is categorized as follows: subsonic flow $0,3 \leq M \leq 0,8$, transonic flow $0,8 \leq M \leq 1,2$, supersonic flow $1,2 \leq M \leq 5$, hypersonic flow $M > 5$, and sonic flow $M = 1$. For incompressible flow, $M < 0,3$ is considered [32].

The Scale-Adaptive Simulation (SAS) model [33] was employed to simulate the turbulence of viscous flow in a transient state. Additionally, Sutherland's law [10], [32] was applied to model the flow viscosity as a function of temperature. Sutherland's law, derived from an approximation of the kinetic theory of gases, accounts for the idealization of intermolecular force potentials and is expressed as equation (7):

$$\frac{\mu}{\mu_o} = \left(\frac{T}{T_o}\right)^{\frac{2}{3}} \frac{T_o + S}{T + S} \quad (7)$$

Where μ is the flow viscosity, $\mu_o = 1,716$ kg/m·s is the reference viscosity, $T_o = 273,11$ K is the reference temperature, and $S = 110,56$ K is the effective temperature. The effective temperature S , also known as the Sutherland constant, is tabulated for various temperature ranges depending on the type of gas.

2.4. Computational solution method

The simulations in ANSYS-Fluent R16.2 were conducted using a density-based solver with a transient

formulation. The 2D computational domain was planar for the planar nozzle and axisymmetric for the conical nozzle. An implicit formulation was employed, with Roe-FDS selected as the flux type. Spatial discretization was performed using a least squares cell-based approach and second-order upwind schemes, while the transient formulation utilized a second-order implicit method. Hybrid initialization was applied, and a residual convergence criterion of 1×10^{-5} was set. The flow field simulations for the nozzle pressure ratio (NPR) range of 1.97–8.91 were resolved in 7,200 to 21,000 iterations.

2.5. Numerical convergence analysis

The computational domains were meshed using the ANSYS-Meshing platform. Four quadrilateral cell grids with varying densities were generated: grid 1 with 19,249 cells, grid 2 with 25,658 cells, grid 3 with 27,311 cells, and grid 4 with 30,736 cells. The Mach number flow field was simulated using the Scale-Adaptive Simulation (SAS) turbulence model [33] for an NPR of 8.91. Among the four grids, grid 4 exhibited the lowest Y -plus (y^+) values, particularly in the shear stress distribution evaluated along the planar nozzle wall (Figure 4a). Regarding shear stress values, the curves for all grids are generally consistent and superimposed, except in the region near the nozzle outlet (Figure 4b).

For the domain meshed with grid 4, the SAS turbulence model [33] was compared with the DES SA [34], DES SST $k-w$ [35], and DES $k-\epsilon$ [36] turbulence models, as illustrated in Figure 4c. The results indicate that the average Mach number at the nozzle exit is similar for the SAS and DES SA turbulence models, as shown in Table 1. The SAS turbulence model was selected for simulating the flow field due to its slight advantage in reducing computational time during iterative calculations. Grid 4 (Figure 3b) features a structured grid composed of quadrilateral cells, with refined regions in the flow zones adjacent to the convergent section ($0 \leq x/L_d \leq 1$) and divergent section ($1 \leq x/L_d \leq 2$), as well as along the walls. Additionally, the grid includes a progressively distributed cell structure in the atmosphere section ($2 \leq x/L_d \leq 8$).

Table 1. Average Mach number at the exit of the planar nozzle for NPR 8.91, evaluated using four different turbulence models

Turbulence model:	SAS [33]	DES SA [34]	DES SST $k-w$ [35]	DES $k-\epsilon$ [36]
Average Mach number:	2.066	2.066	2.065	2.064
Error (%):	0.816	0.816	0.864	0.912

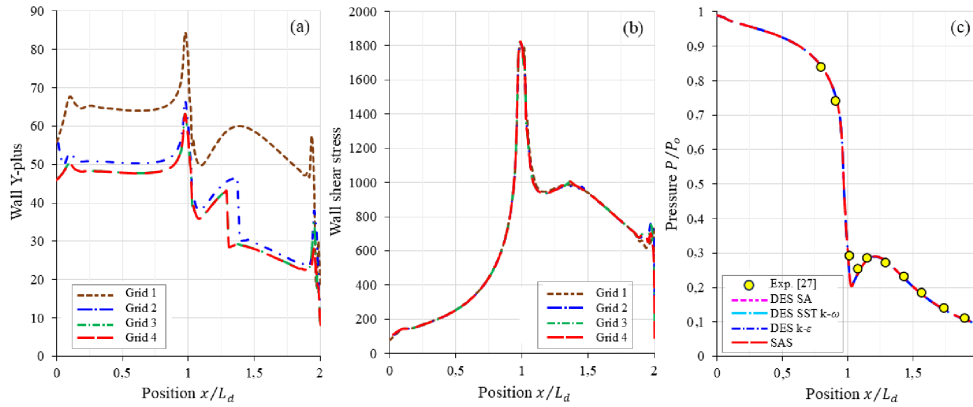


Figure 4. Profiles of curves evaluated along the wall of the planar nozzle: (a) Wall Y-plus, (b) Wall shear stress, and (c) Pressure. Position: convergent section ($0 \leq x/L_d \leq 1$) and divergent section ($1 \leq x/L_d \leq 2$)

3. Results and discussion

This section presents the numerical results for the Mach number flow field (Figure 5) and static pressure distribution (Figure 6) across the NPR range of 1.91 to 8.91. In the flow field visualizations, regions with smaller magnitudes are represented in blue, while regions with larger magnitudes are represented in red. For the planar nozzle, the flow is overexpanded within the NPR range of 1.91 to 7.79 and becomes tailored at NPR 8.91. In contrast, for the conical nozzle, the flow remains overexpanded throughout the entire NPR range of 1.91 to 8.91.

For the planar nozzle, the Mach number flow field (Figure 5a) and static pressure field (Figure 6a) indicate that, at NPR 1.97 and NPR 2.94, the normal shock wave front is located inside the nozzle. For NPR values at or above 3.92, the shock front moves outside the nozzle. In the case of the conical nozzle, the Mach number (Figure 5b) and static pressure (Figure 6b) flow fields reveal that, within the NPR range of 1.97 to 4.88, the normal shock wave front remains inside the nozzle. For NPR values equal to or greater than 5.84, the shock front shifts outside the nozzle.

The evolution of the Mach number flow field and static pressure field for both the planar and conical nozzles demonstrates that the flow regime exhibits distinct behaviors at the same NPR value. As the NPR increases, the shock wave structure evolves, and the flow separation point shifts closer to the nozzle exit.

In the planar nozzle, the distribution of internal shocks is evident both within the nozzle and in the supersonic jet discharging into the atmosphere. However, for the same NPR magnitude, the distribution of internal shocks differs in the conical nozzle. The intensity of shock front displacement is greater in the planar nozzle compared to the conical nozzle.

The trajectories of the centerline profiles for the planar and conical nozzles are illustrated in Figure 7 for Mach number and Figure 8 for static pressure.

In the divergent section ($1 \leq x/L_d \leq 2$) of the planar nozzle (Figure 7a and Figure 8a), velocity and static pressure fluctuations are observed for the NPR range of 2.94 to 8.91. The maximum peak flow velocity occurs at $x/L_d = 1,486$, where the Mach number reaches 2.011, accompanied by a pressure drop of $P/P_o = 0,125$ (Table 2). At $x/L_d = 1,626$, the flow decelerates to Mach 1.819 with a corresponding pressure drop of $P/P_o = 0,169$. At the nozzle outlet, $x/L_d = 2$, the flow velocity reaches Mach 1.991 with a pressure drop of $P/P_o = 0.129$.

In contrast, within the divergent section ($1 \leq x/L_d \leq 2$) of the conical nozzle (Figure 7b and Figure 8b), for the NPR range of 3,92 to 8,91, the peak flow velocity occurs at $x/L_d = 1,577$, reaching Mach 2.844 with a corresponding pressure drop of $P/P_o = 0,034$ (Table 2). The position of this maximum velocity peak is shifted 6.12% downstream compared to the peak position at $x/L_d = 1,486$ in the planar nozzle (Figure 7a). At $x/L_d = 1,633$, the flow decelerates to Mach 2.024 with a pressure drop of $P/P_o = 0.122$, exhibiting a positional shift of 0.43%.

At the outlet of the conical nozzle (Figure 7b and Figure 8b), at the same $x/L_d = 2$ position as the planar nozzle (Figure reffig7a and Figure reffig8a), the flow reaches Mach 2.535 with a corresponding pressure drop of $P/P_o = 0.054$. This represents a 27.32% increase in velocity and a 58.13% decrease in pressure compared to the planar nozzle. It is observed that at the outlet of the conical nozzle, a higher velocity is achieved along the centerline of the flow's central region. However, the overall mass flow rate is lower. This difference is attributed to the throat area of the conical nozzle $A_t = 5,896 \text{ cm}^2$, which restricts the passage of mass flow at sonic velocity. This throat area is 78.79% smaller than that of the planar nozzle $A_t = 27,81 \text{ cm}^2$.

In the atmospheric region ($2 \leq x/L_d \leq 8$) the flow discharge exhibits notable fluctuations. For the planar nozzle (Figures 7a and 8a), at NPR 8.91, the velocity

reaches a maximum peak of Mach 2.522 with a pressure drop of $P/P_o = 0,056$ at $x/L_d = 2,95$. Conversely, the conical nozzle (Figures 7b and 8b) achieves a peak velocity of Mach 2.976 with a pressure drop of $P/P_o = 0,027$ at $x/L_d = 2,408$, reflecting an approximately

18% increase in velocity at this position. Further downstream, the planar nozzle exhibits milder velocity and pressure fluctuations, while these fluctuations are more pronounced in the conical nozzle.

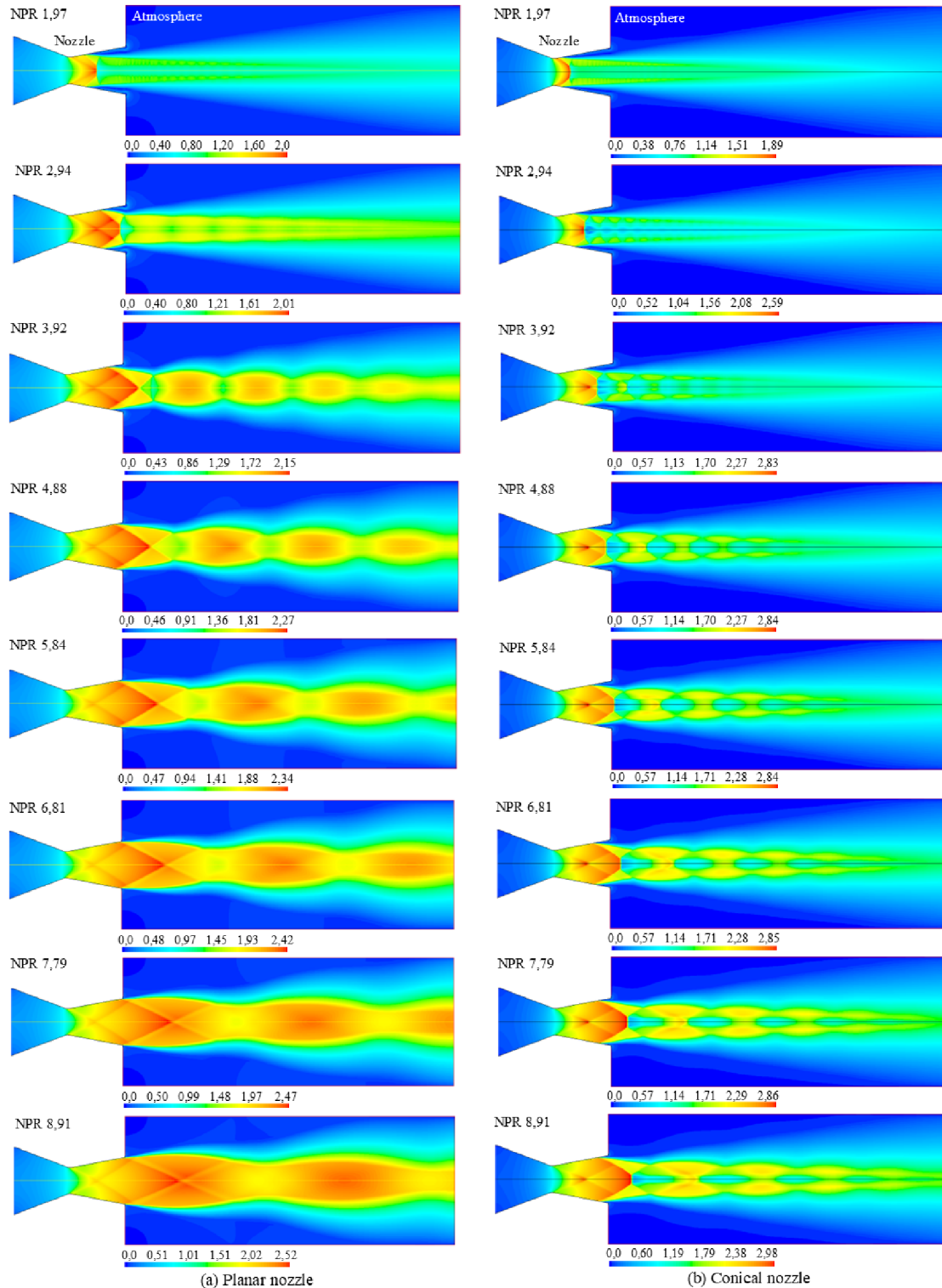


Figure 5. Mach number flow field patterns. Range: NPR 1,97 to NPR 8,91. (a) Planar nozzle. (b) Conical nozzle

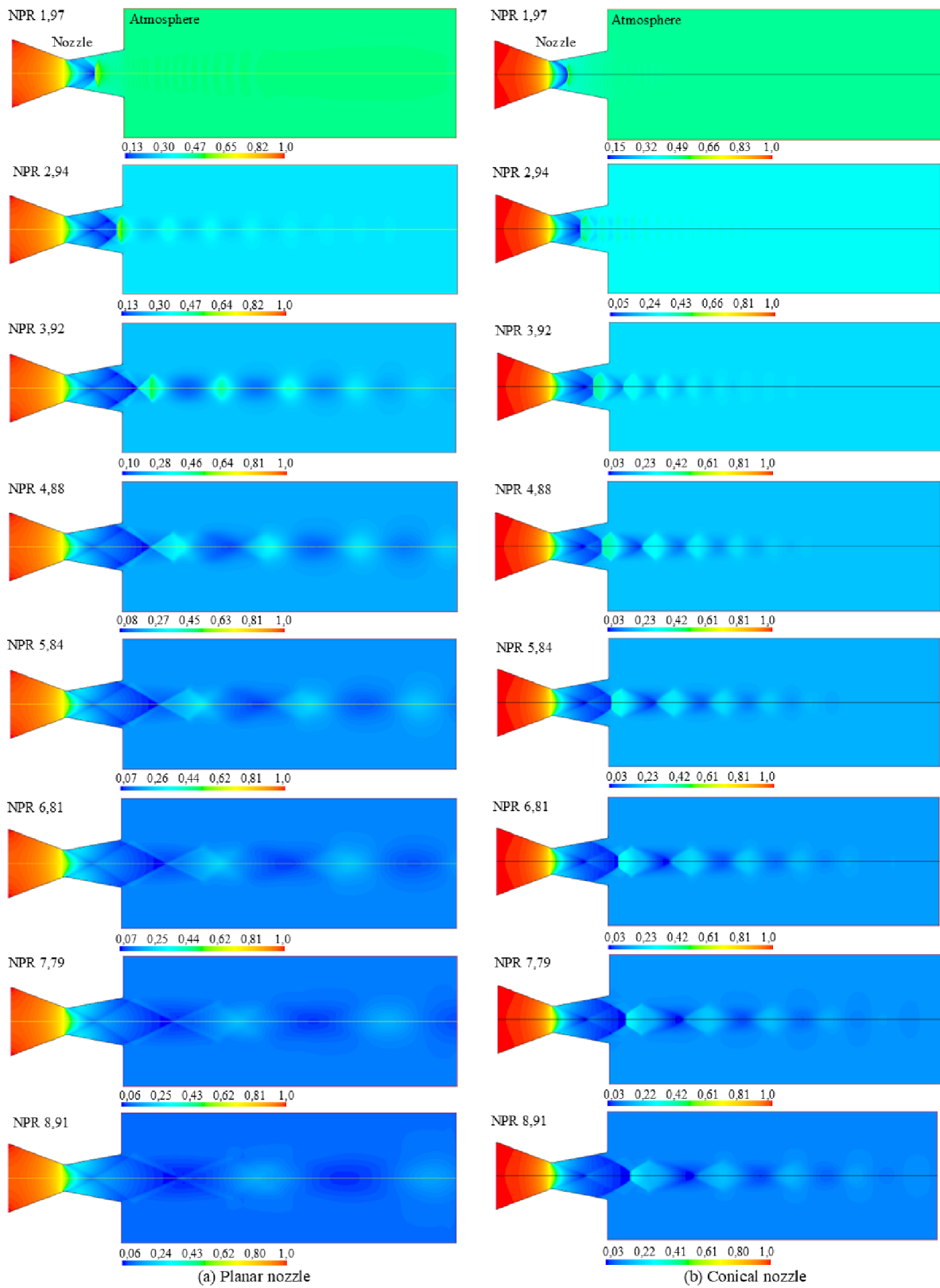


Figure 6. Pressure flow field patterns. Range: NPR 1,97 to NPR 8,91. (a) Planar nozzle. (b) Conical nozzle

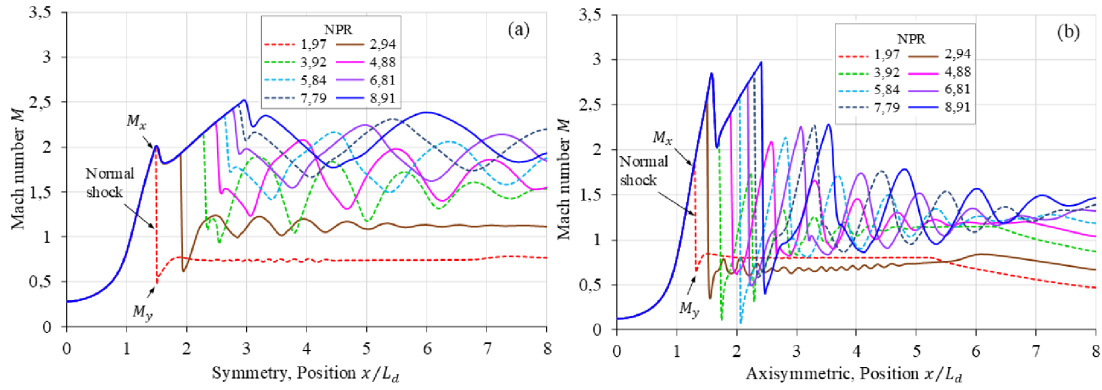


Figure 7. Mach number profile patterns evaluated along the centerline. (a) Planar nozzle. (b) Conical nozzle. Position: convergent section ($0 \leq x/L_d \leq 1$), divergent section ($1 \leq x/L_d \leq 2$) and atmosphere section ($2 \leq x/L_d \leq 8$)

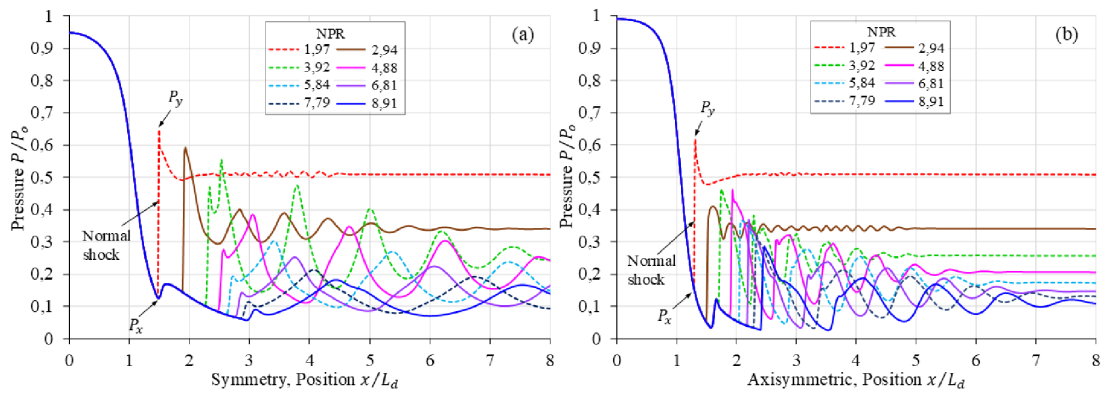


Figure 8. Pressure profile patterns evaluated along the centerline. (a) Planar nozzle. (b) Conical nozzle. Position: convergent section ($0 \leq x/L_d \leq 1$), divergent section ($1 \leq x/L_d \leq 2$) and atmosphere section ($2 \leq x/L_d \leq 8$)

Table 2. Position of the maximum and minimum fluctuations in the central region of the supersonic flow along the centerline of the nozzle’s divergent section

Planar nozzle. Range: NPR 2,94 to NPR 8,91		
Position x/L_d	Mach number M	Position P/P_0
1,486	2,011	0.125
1,626	1,819	0.169
2	1,991	0.129
Conical nozzle. Range: NPR 3,92 to NPR 8,91		
Position x/L_d	Mach number M	Position P/P_0
1,577	2,844	0.034
1,633	2,024	0.122
2	2,535	0.054

Table 3 presents the positions of the normal shock front evaluated along the centerline of the planar nozzle (Figure ??a) and the conical nozzle (Figure ??b). M_x represents the maximum flow velocity at the start of the shock front, while M_y corresponds to the minimum flow velocity at its end. Figures 7 and 8 also show the minimum pressure P_x and the maximum pressure P_y of the shock front for reference.

In the divergent section of the planar nozzle, two

normal shock fronts are observed for NPR 1.97 and NPR 2.94. At the start of the shock front, the flow achieves supersonic velocities ranging from Mach 1.995 to 1.925. By the end of the shock front, the flow transitions to subsonic velocities in the range of Mach 0.473 to 0.610. Outside the nozzle, six normal shock fronts are identified for NPR values of 3.92, 4.88, 5.84, 6.81, 7.79, and 8.91. At the start of these shock fronts, the flow exhibits supersonic velocities ranging from Mach 2.147 to 2.522. At the end of the shock fronts, the flow transitions to transonic and supersonic velocities within the range of Mach 1.072 to 2.221.

In the divergent section of the conical nozzle, four shock fronts are observed for NPR values of 1.97, 2.94, 3.92, and 4.88. At the start of the shock fronts, the flow reaches supersonic velocities ranging from Mach 1.877 to 2.406. By the end of the shock fronts, the flow transitions to subsonic velocities in the range of Mach 0.634 to 0.615. Outside the nozzle, four additional shock fronts are present for NPR values of 5.84, 6.81, 7.79, and 8.91. At the start of these shock fronts, the flow remains supersonic, with velocities ranging from Mach 2.589 to 2.976. At the end of the shock fronts,

the flow transitions to subsonic velocities within the range of Mach 0.072 to 0.4.

It is observed that, at the beginning of the shock fronts for NPR values equal to or greater than 2.94, the flow in the conical nozzle achieves higher supersonic velocities compared to the planar nozzle. At the end of the shock front, the flow in the conical nozzle transitions to subsonic velocity. In contrast, the flow in the planar nozzle exhibits a broader range of behaviors at the end of the shock front, including subsonic, transonic, and supersonic velocities.

The offsets in the positions of the normal shock fronts in the conical nozzle are summarized in Table 3. For the same NPR value, the shock front in the conical nozzle is shifted further to the extreme left compared to the shock front in the planar nozzle. The smallest displacement of the shock front position occurs at NPR 1.97, with the shock onset offset by 12.47% and the shock end by 11.95%. Conversely, the largest displacement is observed at NPR 3.92, with the shock onset offset by 24.44% and the shock end by 25.38%.

Table 3. Positions of normal shock fronts evaluated along the centerline in the divergent section ($1 \leq x/L_d \leq 2$) and atmosphere section ($2 \leq x/L_d \leq 8$)

NPR	Nozzle planar				Conical nozzle			
	Position x/L_d	Mach number M_x	Position x/L_d	Mach number M_y	Position x/L_d	Mach number M_x	Position x/L_d	Mach number M_y
1.97	1.475	1.995	1.497	0.473	1.291	1.877	1.318	0.634
2.94	1.888	1.925	1.935	0.61	1.497	2.587	1.554	0.342
3.92	2.254	2.147	2.336	1.072	1.703	2.128	1.743	0.103
4.88	2.466	2.267	2.57	1.476	1.888	2.406	2	0.615
5.84	2.615	2.344	2.734	1.721	2.045	2.589	2.061	0.072
6.81	2.759	2.415	2.865	1.924	2.179	2.739	2.239	0.486
7.79	2.837	2.466	2.979	2.067	2.286	2.852	2.354	0.579
8.91	2.95	2.522	3.103	2.221	2.408	2.976	2.466	0.4

Table 4. Leftward offset of normal shock front positions in the conical nozzle relative to the planar nozzle

	NPR							
	1.97	2.94	3.92	4.88	5.84	6.81	7.79	8.91
Normal shock front:								
position offset (x/L_d) in percentages (%)								
Start of the shock, M_x:	12.47	20.7	24.44	23.48	21.79	21.02	19.42	18.37
End of the shock, M_y:	11.95	19.68	25.38	22.17	24.61	21.84	20.98	20.52

Similar findings regarding the overexpanded flow and divergent shock structures in planar nozzles have been reported in [6], [23], and in conical nozzles in [15], [27], where the oblique, reflected, and normal shock fronts are influenced by wall geometry and divergence angle. These studies demonstrate that the geometry of supersonic nozzles significantly impacts the development of the flow regime. For the same geometric dimensions projected in the plane, as shown in Figure 2, the planar nozzle and conical nozzle exhibit distinct cross-sectional areas at both the throat and the nozzle outlet [26]. The cross-sectional area of the planar nozzle is larger than that of the conical nozzle, resulting in a smaller mass flow through the throat of the conical nozzle. It is important to note that numerical results are influenced by the simplifications of the mathematical models, the density of cells in the computational mesh, and the turbulence models employed. Consequently, validation with experimental data was essential. The SAS turbulence model, used in the sim-

ulations, was validated to ensure that the numerical results closely approximate the physical phenomena under investigation.

4. Conclusions

Based on the results obtained from computational simulations of the flow field in planar and conical nozzles with a divergence half-angle $\alpha = 10,85^\circ$, which are classified as off-design nozzles, several key observations can be made:

The behavior of the Mach number and static pressure flow fields differs notably between the two nozzle types for the same NPR value. Within the NPR range of 1.97 to 8.91, the shock wave structures evolve distinctly, with their positions and flow separation points progressively shifting toward the nozzle outlet as NPR increases.

In the divergent section of the planar nozzle, the maximum peak flow velocity is observed at $x/L_d =$

1,486, reaching Mach 2.011 with a pressure drop of $P/P_o = 0,125$. In contrast, the conical nozzle achieves its maximum flow velocity at $x/L_d = 1,577$, with Mach 2.844 and a corresponding pressure drop of $P/P_o = 0,034$. This position is shifted 6.12% downstream compared to the $x/L_d = 1,486$ position in the planar nozzle.

In the central region of the flow, the velocity at the nozzle outlet differs significantly between the two geometries. The planar nozzle achieves a flow velocity of Mach 1.991, whereas the conical nozzle reaches Mach 2.535, representing a velocity increase of 27.32% relative to the planar nozzle.

In the atmospheric region at NPR 8.91, where the supersonic jet plume forms, the maximum flow velocity for the planar nozzle is Mach 2.522. In comparison, the conical nozzle achieves Mach 2.976, reflecting an 18% increase in flow velocity. These findings highlight the critical role of the throat area in determining mass flow transit. The larger throat area of the planar nozzle facilitates greater mass flow, while the smaller throat area of the conical nozzle restricts flow, leading to the observed differences in velocity and pressure profiles. This underscores the significant impact of nozzle geometry on flow behavior, particularly in off-design configurations.

Funding

This research was supported by the Vice-Rectorado de Investigación (VRI) of the Universidad Nacional de Ingeniería (UNI), Lima, Peru.

References

- [1] G. P. Sutton and O. Biblarz, *Rocket Propulsion Elements*. John Wiley & Sons, 2016. [Online]. Available: <https://upsalesiana.ec/ing33ar10r1>
- [2] G. Scarlatella, M. Tajmar, and C. Bach, “Advanced nozzle concepts in retro-propulsion applications for reusable launch vehicle recovery: a case study,” in *72nd International Astronautical Congress (IAC), Dubai, United Arab Emirates*, 2021. [Online]. Available: <https://upsalesiana.ec/ing33ar10r2>
- [3] G. Hagemann, A. Preuss, J. Kretschmer, F. Grauer, M. Frey, R. Ryden, and R. Stark, *Technology Investigation for High Area Ratio Nozzle Extensions*. 39th AIAA/ASME/SAE/ASEE Joint Propulsion Conference and Exhibit. [Online]. Available: <https://doi.org/10.2514/6.2003-4912>
- [4] F. J. Malina, “Characteristics of the rocket motor unit based on the theory of perfect gases,” *Journal of the Franklin Institute*, vol. 230, no. 4, pp. 433–454, 1940. [Online]. Available: [https://doi.org/10.1016/S0016-0032\(40\)91348-5](https://doi.org/10.1016/S0016-0032(40)91348-5)
- [5] S. Zivkovic, m. Milinovic, and N. Adamec, “Eksperimentalno i numericko istrazivanje super-sonicnog ravanskog mlaznika sa vektorisanim potiskom mehanickim preprekama,” *FME Transactions*, vol. 42, no. 3, pp. 205–211, 2014. [Online]. Available: <https://doi.org/10.5937/fmet1403205Z>
- [6] C. A. Hunter, “Experimental investigation of separated nozzle flows,” *Journal of Propulsion and Power*, vol. 20, no. 3, pp. 527–532, 2004. [Online]. Available: <https://doi.org/10.2514/1.4612>
- [7] J. D. Anderson, *Hypersonic and High-Temperature Gas Dynamics, Third Edition*. AIAA Education Series, 2019. [Online]. Available: <https://doi.org/10.2514/5.9781624105142.0000.0000>
- [8] K. Q. Zaman and A. F. Fagan, *Flow, noise and thrust of supersonic plug nozzles*. AIAA SCITECH, 2024. [Online]. Available: <https://doi.org/10.2514/6.2024-2305>
- [9] J. H. Ferziger and M. Peric, *Computational Methods for Fluid Dynamics*. Springer Berlin, Heidelberg, 2012. [Online]. Available: <https://doi.org/10.1007/978-3-642-56026-2>
- [10] H. Schlichting and K. Gersten, *Boundary-Layer Theory*. Springer Berlin, Heidelberg, 2016. [Online]. Available: <https://doi.org/10.1007/978-3-662-52919-5>
- [11] S. L. Tolentino, “Comparative analysis of 2d simulations and isentropic equations for compressible flow in experimental nozzles,” *INCAS BULLETIN*, vol. 15, pp. 111–125, 09 2023. [Online]. Available: <https://doi.org/10.13111/2066-8201.2023.15.3.9>
- [12] —, “Empirical equation of the mach number as a function of the stagnation pressure ratio for a quasi- one-dimensional compressible flow,” *FME Transactions*, vol. 51, 03 2023. [Online]. Available: <http://dx.doi.org/10.5937/fme2302149T>
- [13] J. Majdalani and B. Maicke, “Explicit inversion of stodola’s area-mach number equation,” *Journal of Heat Transfer*, vol. 133, p. 071702, 07 2011. [Online]. Available: <http://dx.doi.org/10.1115/1.4002596>
- [14] A. Ferrari, “Exact solutions for quasi-one-dimensional compressible viscous flows in conical nozzles,” *Journal of Fluid Mechanics*, vol. 915, p. A1, 2021. [Online]. Available: <https://doi.org/10.1017/jfm.2020.1158>

- [15] S. L. Tolentino, J. Mírez Tarrillo, and S. Caraballo F., “Numerical analysis of the shock train in conical nozzles with straight-cut throats,” *FME Transactions*, vol. 52, pp. 186–195, 01 2024. [Online]. Available: <http://dx.doi.org/10.5937/fme2402186T>
- [16] P. Krehl and S. Engemann, “August toeppler – the first who visualized shock waves,” *Shock Waves*, vol. 5, no. 1, pp. 1–18, Jun 1995. [Online]. Available: <https://doi.org/10.1007/BF02425031>
- [17] C. Génin, R. Stark, and S. Karl, “Shock system deformation in high mach number rocket nozzles,” in *31st International Symposium on Shock Waves 2*, A. Sasoh, T. Aoki, and M. Katayama, Eds. Cham: Springer International Publishing, 2019, pp. 543–549. [Online]. Available: https://doi.org/10.1007/978-3-319-91017-8_69
- [18] S. B. Verma and C. Manisankar, “Origin of flow asymmetry in planar nozzles with separation,” *Shock Waves*, vol. 24, no. 2, pp. 191–209, Mar 2014. [Online]. Available: <https://doi.org/10.1007/s00193-013-0492-1>
- [19] J. O’stlund and B. Muhammad-Klingmann, “Supersonic flow separation with application to rocket engine nozzles,” *Applied Mechanics Reviews*, vol. 58, no. 3, pp. 143–177, May 2005. [Online]. Available: <https://doi.org/10.1115/1.1894402>
- [20] V. Zmijanović, A. Chpoun, and B. Rasuo, “Flow separation modes and side phenomena in an overexpanded nozzle,” *FME Transactions*, vol. 40, pp. 111–118, 06 2012. [Online]. Available: <https://upsalesiana.ec/ing33ar10r21>
- [21] A. Hadjadj, O. Ben-Nasr, M. Shadloo, and A. Chaudhuri, “Effect of wall temperature in supersonic turbulent boundary layers: A numerical study,” *International Journal of Heat and Mass Transfer*, vol. 81, pp. 426–438, 2015. [Online]. Available: <https://doi.org/10.1016/j.ijheatmasstransfer.2014.10.025>
- [22] R. Zangeneh, “Wall temperature effects on shock unsteadiness in a reattaching compressible turbulent shear layer,” *International Journal of Heat and Fluid Flow*, vol. 92, p. 108876, 2021. [Online]. Available: <https://doi.org/10.1016/j.ijheatfluidflow.2021.108876>
- [23] S. L. Tolentino, J. Mírez, and O. González, “Numerical analysis of the flow field in a planar nozzle for different divergent angles,” *Journal of Mechanical Engineering and Sciences (JMES)*, vol. 16, no. 4, pp. 9241–9252, 2022. [Online]. Available: <https://doi.org/10.15282/jmes.16.4.2022.07.0731>
- [24] R. Arora and A. Vaidyanathan, “Experimental investigation of flow through planar double divergent nozzles,” *Acta Astronautica*, vol. 112, pp. 200–216, 2015. [Online]. Available: <https://doi.org/10.1016/j.actaastro.2015.03.020>
- [25] S. L. Tolentino, J. Mírez, and S. A. Caraballo, “Numerička analiza evolucije udarnog voza u planarnim mlaznicama sa dužinom grla,” *FME Transactions*, vol. 51, no. 4, pp. 595–605, 2023. [Online]. Available: <https://doi.org/10.5937/fme2304595T>
- [26] M. L. Mason, L. E. Putnam, and R. J. Re, *The effect of throat contouring on two-dimensional converging-diverging nozzles at static conditions*. NASA Technical Paper 1704, 1980. [Online]. Available: <https://upsalesiana.ec/ing33ar10r27>
- [27] S. L. Tolentino and J. Mírez, “Efekat dužine grla na obrasce protoka u konusnim mlaznicama van dizajna,” *FME Transactions*, vol. 50, no. 2, pp. 271–280, 2022. [Online]. Available: <https://doi.org/10.5937/fme2201271T>
- [28] B. Wagner and S. Schleichtrien, *Numerical and Experimental Study of the Flow in a Planar Expansion-Deflection Nozzle*. 47th AIAA/ASME/SAE/ASEE Joint Propulsion Conference & Exhibit, 2011. [Online]. Available: <https://doi.org/10.2514/6.2011-5942>
- [29] A. Bourgoing and P. Reijasse, “Experimental analysis of unsteady separated flows in a supersonic planar nozzle,” *Shock Waves*, vol. 14, no. 4, pp. 251–258, Nov 2005. [Online]. Available: <https://doi.org/10.1007/s00193-005-0269-2>
- [30] M. Faheem, A. Khan, R. Kumar, S. Afghan Khan, W. Asrar, and A. M. Sapardi, “Experimental study on the mean flow characteristics of a supersonic multiple jet configuration,” *Aerospace Science and Technology*, vol. 108, p. 106377, 2021. [Online]. Available: <https://doi.org/10.1016/j.ast.2020.106377>
- [31] (ANSYS-Fluent). (2023) Ansys fluent theory guide 2020r1. Ansys Innovation Space. [Online]. Available: <https://upsalesiana.ec/ing33ar10r32>
- [32] F. M. White, *Fluid Mechanics*. McGraw Hill, 2011. [Online]. Available: <https://upsalesiana.ec/ing33ar10r33>
- [33] Y. Egorov, F. R. Menter, R. Lechner, and D. Cokljat, “The scale-adaptive simulation method for unsteady turbulent flow predictions. part 2: Application to complex flows,” *Flow, Turbulence and Combustion*, vol. 85, no. 1, pp. 139–165, Jul 2010. [Online]. Available: <https://doi.org/10.1007/s10494-010-9265-4>

- [34] P. R. Spalart, S. Deck, M. L. Shur, K. D. Squires, M. K. Strelets, and A. Travin, "A new version of detached-eddy simulation, resistant to ambiguous grid densities," *Theoretical and Computational Fluid Dynamics*, vol. 20, no. 3, pp. 181–195, Jul 2006. [Online]. Available: <https://doi.org/10.1007/s00162-006-0015-0>
- [35] F. Menter, M. Kuntz, and R. B. Langtry, "Ten years of industrial experience with the sst turbulence model," *Heat and Mass Transfer*, vol. 4, 01 2003. [Online]. Available: <https://upsalesiana.ec/ing33ar10r36>
- [36] S. Tsan-Hsing, W. L. William, S. Aamir, Y. Zhigang, and Z. Jiang, "A new k- ϵ eddy viscosity model for high reynolds number turbulent flows," *Computers & Fluids*, vol. 24, no. 3, pp. 227–238, 1995. [Online]. Available: [https://doi.org/10.1016/0045-7930\(94\)00032-T](https://doi.org/10.1016/0045-7930(94)00032-T)